

Band structure and Klein paradox for a pn junction in ABCA-tetralayer graphene

Abderrahim EL MOUHAFID^{1,*} and Ahmed JELLAL^{1,2,†}

¹*Laboratory of Theoretical Physics, Faculty of Sciences,
Chouaib Doukkali University, PO Box 20, 24000 El Jadida, Morocco*

²*Saudi Center for Theoretical Physics, Dhahran, Saudi Arabia*

(Dated: 28 février 2022)

We investigate the band structure of ABCA-tetralayer graphene (ABCA-TTLG) subjected to an external potential V applied between top and bottom layers. Using the tight-binding model, including the nearest t and next-nearest-neighbor t' hopping, low-energy model and two-band approximation model we study the band structure variation along the lines $\Gamma - M - K - \Gamma$ in the first Brillouin zone, electronic band gap near Dirac point K and transmission properties, respectively. Our results reveal that ABCA-TTLG exhibits markedly different properties as functions of t' and V . We show that the hopping parameter t' changes the energy dispersion, the position of K and breaks sublattice symmetries. A sizable band gap is created at K , which could be opened and controlled by the applied potential V . This gives rise to 1D-like van Hove singularities (VHS) in the density of states (DOS). We study the relevance of the skew hopping parameters γ_3 and γ_4 to these properties and show that for energies $E \gtrsim 6\text{meV}$ their effects are negligible. Our results are numerically discussed and compared with the literature.

PACS numbers: 72.80.Vp, 73.21.Ac, 73.22.Pr

I. INTRODUCTION

Generally, graphene can be stacked in various ways to form multilayered graphenes (MLG) with different physical properties. Typical graphene stacking includes Order, Bernal (AB), and Rhombus stacking (ABC)^{1–6}. In Order stacking, all carbon atoms of each layer are well-aligned. For AB and ABC stacking, a cycle period is constituted by two layers and three layers of non-aligned graphene, respectively. It has been showed that the properties of graphene like band structure, band gap, transport properties, optical properties and density of state depend on the way how graphene is stacked^{1,7–17} and also on the application of external sources^{1,8,18}. Indeed, Aoki and Amawashi showed that the AB-stacked MLG is a semi-metal with an electrically tunable band overlap, while the ABC-stacked MLG is a semiconductor with an electrically tunable band gap¹. Mak *et al.* experimentally investigated the electronic structure of few-layer graphene samples with crystalline order by infrared absorption spectroscopy for photon energies¹⁰. Lu *et al.* investigated the influence of AB stacking on the optical properties of MLG in an electric field¹⁴. Ben *et al.* studied the influence of ABC stacking on the Klein and anti-Klein tunneling of MLG in an external potential¹⁵. As a consequence, MLG exhibits the rare behavior of crystal structure modification, and hence modification of electronic properties, via the application of the potential, electric and magnetic fields.

In the present work, we study the electronic properties of ABCA-TTLG in the presence of an external potential V applied between top and bottom layers. These properties are explored by employing the tight-binding Hamiltonian, low-energy and two-band approximation models. They are strongly dependent on the geometric structure and the applied potential V . The application

of V remarkably modifies the energy dispersions, causes the subbands anticrossing, changes the subbands spacing and induces the oscillating bands. Here we are limited ourselves to next-nearest-neighbor hoppings t' and neglected other less important hoppings that are present in ABCA-TTLG. We show that t' affects the density of states (DOS) of ABCA-TTLG. At low energy the Klein (KT) and anti-Klein (AKT) tunneling are analyzed.

The manuscript is organized as follows. In Sec. II, we introduce the tight-binding Hamiltonian, low-energy and two-band approximation models to calculate the band structure of ABCA-TTLG. Sec. III and IV are devoted to numerical analysis and discussion of the band structure behavior and transmission probabilities for electrons impinging on a potential step (pn junction). Our main conclusions are summarized in Sec. V.

II. THE HAMILTONIAN MODEL

We consider a lattice of ABCA-TTLG consists of four coupled layers^{5,15}, each with carbon atoms arranged on a honeycomb lattice, including pairs of inequivalent sites $\{\alpha_1, \beta_1\}$, $\{\alpha_2, \beta_2\}$, $\{\alpha_3, \beta_3\}$, and $\{\alpha_4, \beta_4\}$ in the top, center, and bottom layers, respectively. The layers are arranged as shown in Fig. 1(a) such that pairs of sites β_1 and α_2 , β_2 and α_3 and β_3 and α_4 , lie directly above or below each others. The different sublattices α_i and β_i are represented by darkred and teal solid balls, respectively. In order to write down an effective mass Hamiltonian, we adapt the Slonczewski-Weiss-McClure parameterization of tight-binding couplings of bulk graphite². We include parameters $\gamma_0, \gamma_1, \gamma_2, \gamma_3$ and γ_4 , where γ_0 the intralayer coupling $\alpha_i \leftrightarrow \beta_i$ ($i = 1, 2, 3, 4$), γ_1 the interlayer coupling $\beta_i \leftrightarrow \alpha_{i+1}$ ($i = 1, 2, 3$), γ_2 the interlayer coupling $\alpha_i \leftrightarrow \alpha_{i+2}$ and $\beta_i \leftrightarrow \beta_{i+2}$ ($i = 1, 2$), γ_3 the interlayer

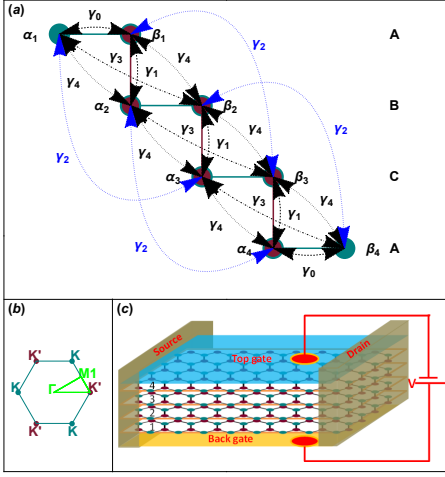


FIGURE 1: (Color online) (a) Tight-binding diagram for four stacking types ABCA-TTLG showing the Slonczewski-Weiss-McClure parameterization² of relevant couplings γ_0 to γ_4 . (b) Schematic of the hexagonal Brillouin zone (BZ) with two inequivalent valleys K and K' . (c) Schematic representation of ABCA-TTLG junction. There is an electrostatic potential difference $V = 2U_0$ between top and bottom layers. Sublattices α_i and β_i are represented in different colors.

coupling between α_i and β_{i+1} ($i = 1, 2, 3$), γ_4 the inter-layer coupling $\alpha_i \leftrightarrow \alpha_{i+1}$ and $\beta_i \leftrightarrow \beta_{i+1}$ ($i = 1, 2, 3$). For typical values, we quote² $\gamma_0 \approx 3.16\text{eV}$, $\gamma_1 \approx 0.39\text{eV}$, $\gamma_2 \approx -0.020\text{eV}$, $\gamma_3 \approx 0.315\text{eV}$ and $\gamma_4 \approx 0.044\text{eV}$. These interatomic coupling parameters are depicted in Fig. 1(a). The contribution of the skew hopping parameter γ_3 results in the so called^{19,20} trigonal warping, an effect occurring only at very low energy ($E \lesssim 6\text{meV}$) which will be discussed in Sec III B. The parameter γ_4 has an even lower impact on the electronic properties, see Sec III B. Therefore, we will often neglect these two γ -parameters in Sec III A and III C. There is a degeneracy point at each of two inequivalent corners K and K' of the hexagonal first Brillouin zone, also referred to as valleys, Fig. 1(b). Near the centre of each valley, there are eight electronic bands. In the basis $\{\alpha_1, \beta_1, \alpha_2, \beta_2, \alpha_3, \beta_3, \alpha_4, \beta_4\}$ the electronic properties for ABCA-TTLG are then obtained from the following Hamiltonian matrix⁵

$$\mathcal{H}(\mathbf{k}) = \begin{bmatrix} \mathcal{H}_1(\mathbf{k}) & \Gamma_1 & \Gamma_2 & 0 \\ \Gamma_1^\dagger & \mathcal{H}_2(\mathbf{k}) & \Gamma_1 & \Gamma_2 \\ \Gamma_2^\dagger & \Gamma_1^\dagger & \mathcal{H}_3(\mathbf{k}) & \Gamma_1 \\ 0 & \Gamma_2^\dagger & \Gamma_1^\dagger & \mathcal{H}_4(\mathbf{k}) \end{bmatrix}, \quad (1)$$

where the interlayer couplings Γ_1 and Γ_2 are given by

$$\Gamma_1 = \begin{bmatrix} -v_4 f(\mathbf{k}) & v_3 f^\dagger(\mathbf{k}) \\ \gamma_1 & -v_4 f(\mathbf{k}) \end{bmatrix}, \quad \Gamma_2 = \begin{bmatrix} 0 & \gamma_2/2 \\ 0 & 0 \end{bmatrix} \quad (2)$$

with $v_{3,4} = v_F \gamma_{3,4}/\gamma_0$ are related to the skew hopping parameters, $v_F = 3a\gamma_0/(2\hbar)$ is the Fermi velocity in terms of the in-plane nearest neighbor hopping γ_0 , a is the lattice constant. The 2×2 matrix $\mathcal{H}_i(\mathbf{k})$ describes the in-

tralayer processes for ABCA-TTLG is

$$\mathcal{H}_i(\mathbf{k}) = \begin{pmatrix} V_i & f(\mathbf{k}) \\ f^\dagger(\mathbf{k}) & V_i \end{pmatrix}, \quad (3)$$

$i = 1, 2, 3, 4$ labeling the graphene layers, V_i describe an external potential in each layers, $f(\mathbf{k})$ is a momentum space representation of intersublattice hopping processes for electrons with wave vector \mathbf{k} . In the framework of a tight-binding approximation (see Sec. III A), $f(\mathbf{k})$ is given by^{21–23}

$$f(k) = -t' - t(e^{-ik \cdot a_1} + e^{-ik \cdot a_2}), \quad (4)$$

where $a_1 = (a/2)(-\sqrt{3}e_x + e_y)$ and $a_2 = (a/2)(\sqrt{3}e_x + e_y)$ are basis vectors of the triangular Bravais lattice, in terms of the lattice constant a , t is the nearest-neighbor hopping energy (hopping between different sublattices), and t' the next nearest-neighbor hopping integral (hopping in the same sublattice). The angular dependence of $f(k)$ in Eq. 4 is called trigonal warping because it leads to a deformation of the form of the Fermi line around the centre of each valley. This deformation increases with an increase of the absolute value of the wave vector. In ABCA-TTLG, a second cause of trigonal warping is the parameter γ_3 describing direct interlayer coupling between α_i and β_{i+1} ($i = 1, 2, 3$), leading to an effective velocity $v_3 = v_F \gamma_3/\gamma_0$. In the low-energy model (see Sec. III B), $f(\mathbf{k})$ is

$$f(\mathbf{k}) = \hbar v_F(k_x - ik_y), \quad (5)$$

where $\mathbf{k} = (k_x, k_y)$ is the two dimensional momentum operator. The applied potential V_i can be varied by gating the sample with top and back gates (see Fig. 1(c)). This is

$$V_i = \begin{cases} U_0 & \text{for } i = 1 \text{ (layer 1)} \\ 0 & \text{for } i = 2 \text{ (layer 2)} \\ 0 & \text{for } i = 3 \text{ (layer 3)} \\ -U_0 & \text{for } i = 4 \text{ (layer 4)}, \end{cases} \quad (6)$$

where U_0 describes a potential difference between layers 1 and 4.

III. BAND STRUCTURE

A. Tight-binding model

In order to calculate the full dispersion of ABCA-TTLG we numerically diagonalize the Hamiltonian Eq. (1). The resulting diagonal matrix then contains eight distinct entries corresponding to the energy bands compared with monolayer, AB-BL and ABC-TLG which contains two, four and six bands, respectively. These eight bands are plotted in Fig. 2, 3 and 4. In Fig. 2, we show the typical behavior of the band structure dependence of next-nearest-neighbor hopping t' for fixed

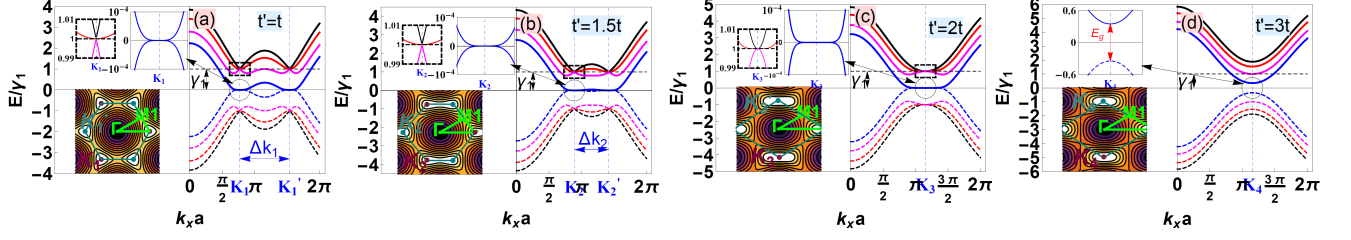


FIGURE 2: (Color online) Band structure of ABCA-TTLG for $k_y = 0$ and $U_0 = 0$. The blue, magenta, red and black curves correspond to the tight-binding model. The solid curves correspond to the conduction bands and the dashed curves correspond to the valance bands. (a) $t' = t$, (b) $t' = 1.5t$, (c) $t' = 2t$ and (d) $t' = 3t$. The vertical dashed lines indicates the position of the points K .

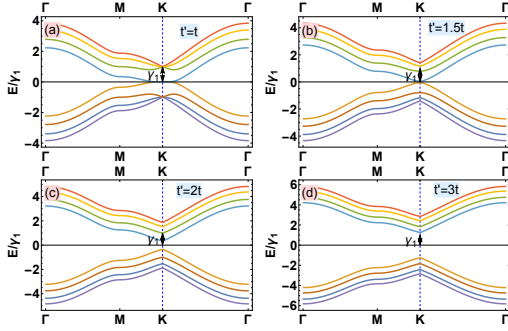


FIGURE 3: (Color online) Band structure of ABCA-TTLG along the lines $\Gamma - M - K - \Gamma$ in the first BZ for $U_0 = 0$, (a) $t' = t$, (b) $t' = 1.5t$, (c) $t' = 2t$, (d) $t' = 3t$. K , Γ and M are, respectively, the corner, the center and the middle point between two corners in the hexagonal BZ as shown in Fig. 1(b).

nearest neighbor t and applied potential $U_0 = 0$. For $t' = t$ the energy vanishes at two points located at the Dirac corners K_1 and K'_1 of the hexagonal BZ spaced by $\Delta K_1 = K'_1 - K_1$ (see Fig. 2(a)). For $2t > t' > t$, the Dirac points approach each other, their distance varies as $\Delta K_2 = K'_2 - K_2 < \Delta K_1$, the Dirac cones become anisotropic (deformed honeycomb lattice) (see Fig. 2(b)). For $t' = 2t$, the two Dirac points merge into a single point at $K_3 = K'_3$ (see Fig. 2(c)). For $t' > 2t$, a gap opened $E_g \simeq 0.694\text{eV}$ between the conduction and valance bands, and the two Dirac points coincide at $K_4 = K'_4$ (see Fig. 2(d)). We notice that for $t' < 2t$ and $U_0 = 0$ the band structure of ABCA-TTLG in our Tight-binding model consists of a set of four pairs cubic of bands, one of them touching each other at the points K and K' , and the other three crossing at the energy $E = \pm\gamma_1$. These two bands intersect exactly at E_F which corresponds to the special point K in the reciprocal space of the hexagonal lattice. The insets of Fig. 2 show the zoom of the bands at the Dirac point and the deformation of hexagonal Brillouin zone (lattice) by variation of the next nearest-neighbor hopping t' .

For a more understanding of the effects of the next nearest neighbors t' on band structure of ABCA-TTLG

we show in Fig. 3 the π bands for different values of t' along the lines $\Gamma - M - K - \Gamma$ in the first BZ. From this Figure it is very clear that the presence of the parameters t' (as t' increases) introduces a band gap on the band structure.

To illustrate the effects of the potential U_0 on the band structure of ABCA-TTLG in the tight-binding model we plot it versus the transverse wave vector k_x in Fig. 4 for some values the potential height $U_0 = 0.3, 1, 1.5$ with $t' = t$. The Bravais lattice retains its shape even if U_0 is strong but U_0 contribute to the opening of a gap between the conduction and valance bands. Note that $\Delta K_1 = K'_1 - K_1$ remains unchangeable. More interesting features appear when zooming into the low energy regime around the point K see Sec. III B.

In Fig. 5, the influence of next-nearest-neighbor t' hopping on electronic DOS in ABCA-TTLG is shown. The DOS have a zero value at the Fermi energy and ten sharp van Hove singularities (VHS) appear at the onset of each subband. We also see, as in the spectrum, an apparent symmetry for positive and negative VHS in the DOS. This also implies zero-gap semiconductor with semi metallic behavior. In addition, sharp peaks in the DOS are observed, which are the characteristic signatures of the one-dimensional (1D) nature of conduction within a 1D system. We conclude that by varying t' , VHS can be brought to accessible energies, which is one of the important features of the ABCA-TTLG.

B. Low-energy model

The band gap is an intrinsic property of semiconductors, which indeed hugely determines the transport and the optical properties. It should have a key role in modern device industry and technology. In this section, we focus on the sensitivity of the band structure of ABCA-TTLG at low-energy by varying the applied potential V defined in Eq. 6 between the top and the bottom layer. Using similar approach as before, we show in Fig. 6 the 2D (upper row) band structure at point K and the corresponding 3D plot (lower row) of the effective Hamiltonian derived from Eq. 1 where $f(\mathbf{k})$ is given by Eq. 5. The

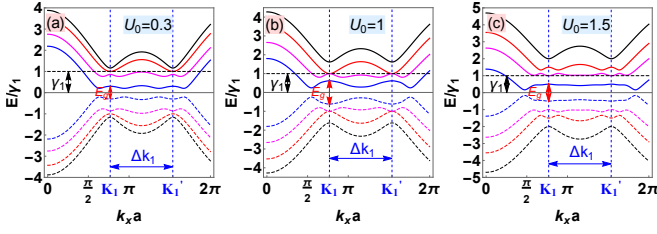


FIGURE 4: (Color online) Band structure of ABCA-TTLG for $k_y = 0$ and $t' = t$. The blue, magenta, red and black curves correspond to the tight-binding model. The solid curves correspond to the conduction bands and the dashed curves correspond to the valence bands. (a) $U_0 = 0.3$, (b) $U_0 = 1$, (c) $U_0 = 1.5$. The vertical dashed line indicates the position of the Dirac point K .

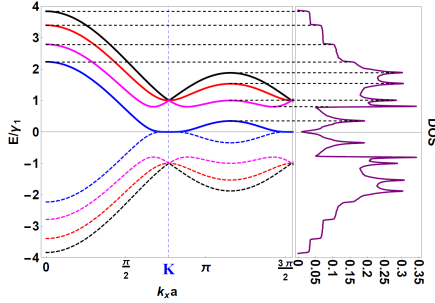


FIGURE 5: (Color online) Band structure of ABCA-TTLG presented in Fig. 2(a) from tight-binding model, with the right hand side panel exhibiting the corresponding DOS. Sharp spikes in the DOS are VHS. The positive VHS are indicated by the dashed lines. The energy dispersion relations are presented in the energy interval $[-4\gamma_1, 4\gamma_1]$ in dimensionless units. The Fermi level is located at zero energy.

potential is $\pm U_0$ for the top and bottom layer. The dashed curves also account for the skew hopping parameters defined in Fig. 1(a) while the solid curve considers only nearest-neighbor interlayer hopping t' . It is clear that at high energy $E > 6\text{meV}$ the effect of the skew hopping parameters γ_3 and γ_4 to these band structures depicted in Fig. 6 is negligible (see Fig. 7(a)). That is why we did not take into consideration their effects on the band gaps. Trigonal warping due to γ_3 becomes particularly relevant at very low energy of the order of 6meV . Fig. 7(b) shows contour plots of the lower electron band at $U_0 = 0$, showing that the band is trigonally warped, and the contour splits into three pockets at low energy. The detailed band structure and its relation to the band parameters will be studied in the present sections.

For $U_0 = 0$ the spectrum consists of a set of four pairs cubic of bands, one of them touching each other at the point K and the other three crossing at an energy $E = \pm\gamma_1$ above (below) K , as shown in Fig. 6(a). However, for $U_0 \neq 0$ the location of the fundamental gap shifted, in BZ, from K to finite values of K , similar to what was observed in the gated multi-layer graphene^{12,13} (see Fig. 6(b, c)). From these figures, four pairs of bands

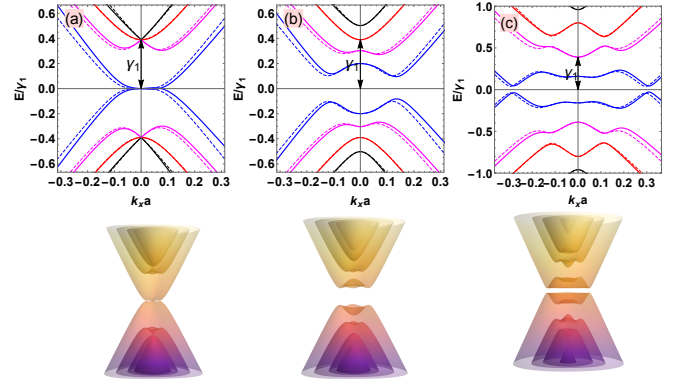


FIGURE 6: (Color online) Band structure near the Dirac point K , calculated in the low-energy model of ABCA-TTLG (top), with the corresponding 3D (below), when the potential difference (a) $U_0 = 0$, (b) $U_0 = 0.2$ and (c) $U_0 = 0.8$. The solid curves correspond to the band structure in the first neighbor approximation (i.e., γ_0 and γ_1 only) and the dashed curves correspond to the band structure in the full parameters model. A band gap is previously created by application of an external potential difference between top and bottom layers.

hybridize and repel each other and a sizable band gap is created at K , which could be opened and controlled by $\pm U_0$. The repelling of the two bands creates band gaps $E_{gi} = E_{ci} - E_{vi}$ with $i = 1, 2, 3, 4$. We denote the pair of highest (lowest) bands near the Dirac point as the conduction (valence) bands. Around K and for $k_y = 0$, these bands exhibit several local maxima and minima as the potential difference U_0 is increased (see Fig. 6(b, c) and Tab. I). Always they are symmetric with respect to E_F . Therefore, the band gaps E_{gi} are strongly dependent on U_0 and are given by

$$E_{g1} = \begin{cases} -U_0 + \sqrt{U_0^2 + 4\gamma_1^2} & \text{for } U_0 > \frac{\gamma_1}{\sqrt{2}} \\ 2U_0 & \text{for } U_0 \leq \frac{\gamma_1}{\sqrt{2}}, \end{cases} \quad (7)$$

$$E_{g2} = \begin{cases} 2\gamma_1 & \text{for } U_0 \geq \gamma_1 \\ 2U_0 & \text{for } \frac{\gamma_1}{\sqrt{2}} < U_0 < \gamma_1 \\ -U_0 + \sqrt{U_0^2 + 4\gamma_1^2} & \text{for } U_0 \leq \frac{\gamma_1}{\sqrt{2}}, \end{cases} \quad (8)$$

$$E_{g3} = \begin{cases} 2U_0 & \text{for } U_0 \geq \gamma_1 \\ 2\gamma_1 & \text{for } U_0 < \gamma_1, \end{cases} \quad (9)$$

$$E_{g4} = \begin{cases} 2U_0 & \text{for all } U_0, \end{cases} \quad (10)$$

These four bands are illustrated in Fig. 8 which clearly define a better understanding of the band structure of ABCA-TTLG dependence on the band gap. The gaps are measured in units of γ_1 . Our main result shows that the first band gap E_{g1} initially increases and falls as U_0 increased. E_{g1} is zero at $U_0 = 0$ (P_1 point) and reaches a maximum 1.414eV as U_0 reaches $0.707\text{V}/\text{\AA}$ (P_2 point). The second band gap E_{g2} exhibits one local minima at $U_0 = 0.707\text{V}/\text{\AA}$ (P_2 point) and two local maxima who have the same gap energy 2eV at $U_0 = 0$ (P_4) and at $U_0 = 1\text{V}/\text{\AA}$ (P_3), and then remains constant. E_{g3} varies

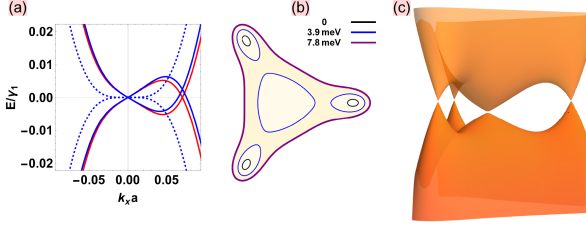


FIGURE 7: (Color online) Energy spectrum of ABCA-TTLG near one of the Dirac point K at low energy. The solid blue curve corresponds to the spectrum accounting for all inter-atomic hopping parameters considered in Fig 1, the solid red curve corresponds to $\gamma_4 = 0$, and the dashed curve accounts only for γ_0 and γ_1 .

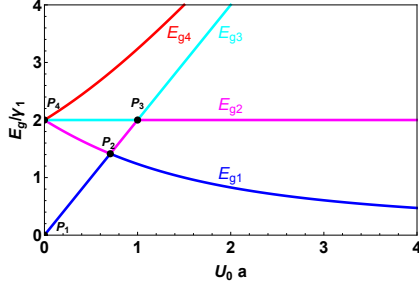


FIGURE 8: (Color online) Band gap of ABCA-TTLG around the Dirac point K for $k_y = 0$ versus the potential difference U_0 .

steadily until U_0 reaches $1V/\text{\AA}$ (P_3) and then increases monotonically when U_0 increases. As long as U_0 increase the band gap E_{g4} continuously increased.

In general, for the ABCA-TTLG the coordinates of the points P_1 , P_2 , P_3 and P_4 illustrated in Fig. 8 are given by $P_1(0,0)$, $P_2(\gamma_1/\sqrt{2}, \sqrt{2}\gamma_1)$, $P_3(\gamma_1, 2\gamma_1)$ and $P_4(0, 2\gamma_1)$, which are strongly dependent on γ_1 . We note that the behavior of the minimum band gap E_{g1} in ABCA-TTLG is similar to ABC-TLG^{5,18}, which increases by increasing U_0 with band gaps below a critical value, and decreases with band gaps above this critical value. By contrast, in AB-BLG^{5,24} the situation is completely different because E_{g1} increases as U_0 increases.

U_0	0	0.5	0.7	1	1.5	3
$E_{g1}(\text{ABCA})$	0	1	1.4	1.236	1	0.605

TABLE I: Several values of the energy gap E_{g1} for a several values of U_0 .

C. Two-band approximation model

The same as for AB-BLG and ABC-TLG, it is possible to introduce the effective two-band description at low energy approximation for the ABCA-TTLG. This two component Hamiltonian was derived in²⁵⁻²⁷ and is only

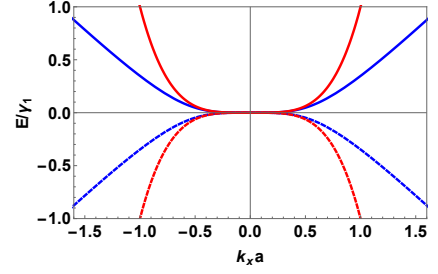


FIGURE 9: Band structure of ABCA-TTLG around the Dirac point K for $k_y = 0$. The blue curves correspond to the low energy model (Eq. 1) and the red curves correspond to the two band approximation model (Eq. 11).

valid as long as the electronic density is low enough, that is, when the Fermi energy is much smaller than γ_1 ($E \ll \gamma_1$). We use similar analysis to that previously described in Ref.²⁵, which yields the Hamiltonian¹⁵

$$\mathcal{H}'(\mathbf{k}) = \begin{bmatrix} V & \alpha(k_x - ik_y)^4 \\ \alpha(k_x + ik_y)^4 & -V \end{bmatrix}, \quad (11)$$

where $\alpha = \frac{(\hbar v_F)^4}{\gamma_1^3}$. In the two band approximation model, the Hamiltonian in Eq. 11 has a plane wave solution given by two propagating waves, one right and one left moving, and six evanescent waves. The wave vectors of these plane waves are the solutions of the equation

$$\alpha^2(k_j^2 + k_y^2)^4 + V^2 = \varepsilon^2, \quad (12)$$

where $k_y = \varepsilon^{1/4} \sin(\phi_k)$ is the transverse wave vector, $\phi_k = \arctan(k_y/k_x)$ is the angle of the wave vector \mathbf{k} with the normal chosen perpendicular to the pn junction. The solution of this equation is $\pm k_j$ with four different values for k_j and the dispersion relation is given by

$$\varepsilon_{\pm} = \pm \sqrt{\alpha^2(k_j^2 + k_y^2)^4 + V^2}. \quad (13)$$

The validity of this approximation is presented in Fig. 9 where we show the dispersion relation obtained in the low energy model (blue curves) and the dispersion relation obtained from the Hamiltonian in the two bands model (red curves). We clearly see that for $E \ll \gamma_1$ the two band spectrum for the low-energy model are in good agreement with the two band spectrum for low energy Eq. 11.

IV. TRANSMISSION PROBABILITY

In this paragraph, we focus on the transmission probability through a pn junction in the two band approximation model (Eq. 11) and adopt the same approach used by Ben *et al.*¹⁵. The eigenstates of these 2×2 Hamiltonians are eight-component spinors consisting of a superposition of four times two oppositely propagating or evanescent waves characterized by four distinct wave

vectors denoted as k_1, k_2, k_3 and k_4 . For a system that is translational invariant in the y direction, the energy and k_y dependence on these wave vectors k_i can be found from

$$\det [\mathcal{H}'(\mathbf{k}) - EI_8] = 0, \quad (14)$$

and $\mathcal{H}(\mathbf{k})$ is given by Eq. 11. The eigenstates solution can be written as a product of matrices,

$$\psi(x, y) = \mathcal{M} \mathcal{W}(x, y) \mathcal{C}, \quad (15)$$

where \mathcal{M} is a 8×2 matrix expressing the relative importance of the different components of the spinor that can be constructed by solving the Dirac equation $\mathcal{H}(\mathbf{k})\psi(x, y) = E\psi(x, y)$. The matrix \mathcal{M} is given by

$$\mathcal{M} = \begin{bmatrix} 1 & 1 & 1 & 1 & 1 & 1 & 1 & 1 \\ f_1^+ & f_1^- & f_2^+ & f_2^- & f_3^+ & f_3^- & f_4^+ & f_4^- \end{bmatrix}, \quad (16)$$

where $f_j^\pm = \frac{(\pm k_j + i k_y)^4}{\varepsilon}$ and the matrix \mathcal{W} is

$$\mathcal{W}(x, y) = \text{diag} [e^{ik_1 x}, e^{-ik_1 x}, e^{ik_2 x}, e^{-ik_2 x}, e^{ik_3 x}, e^{-ik_3 x}, e^{ik_4 x}, e^{-ik_4 x}] e^{ik_y y}, \quad (17)$$

due to the translational symmetry in the y direction, the y dependency is incorporated in an exponential phase factor and will be ignored from this point on. We denote the four component vector \mathcal{C} as

$$\mathcal{C} = [a_1^+, a_1^-, a_2^+, a_2^-, a_3^+, a_3^-, a_4^+, a_4^-]^T, \quad (18)$$

where the subscript $i = 1, \dots, 4$ refers to the corresponding wave vector and the superscript plus/minus indicates the right/left propagating or evanescent states. The boundary conditions of the system under consideration will determine which of the components of vector \mathcal{C} are zero. To find the transmission probability for a pn junction, one has to equate the plane wave solutions and all

the derivatives up to 3^{th} order of the region before the junction (region I) with those of the region behind it (region II) at the junction's edge at $x = 0$, giving rise to a set of four two component equations¹⁵

$$\begin{cases} \mathcal{M}_I \mathcal{W}_I \mathcal{C}_I = \mathcal{M}_{II} \mathcal{W}_{II} \mathcal{C}_{II} \\ \mathcal{M}_I \frac{\partial \mathcal{W}_I}{\partial x} \mathcal{C}_I = \mathcal{M}_{II} \frac{\partial \mathcal{W}_{II}}{\partial x} \mathcal{C}_{II} \\ \mathcal{M}_I \frac{\partial^2 \mathcal{W}_I}{\partial x^2} \mathcal{C}_I = \mathcal{M}_{II} \frac{\partial^2 \mathcal{W}_{II}}{\partial x^2} \mathcal{C}_{II} \\ \mathcal{M}_I \frac{\partial^3 \mathcal{W}_I}{\partial x^3} \mathcal{C}_I = \mathcal{M}_{II} \frac{\partial^3 \mathcal{W}_{II}}{\partial x^3} \mathcal{C}_{II}, \end{cases} \quad (19)$$

where the matrix \mathcal{W} is evaluated at $x = 0$. This leads to the matrix

$$\mathcal{M} = \begin{bmatrix} 1 & 1 & 1 & 1 & 1 & 1 & 1 & 1 \\ f_1^+ & f_1^- & f_2^+ & f_2^- & f_3^+ & f_3^- & f_4^+ & f_4^- \\ ik_1 & -ik_1 & ik_2 & -ik_2 & ik_3 & -ik_3 & ik_4 & -ik_4 \\ ik_1 f_1^+ & -ik_1 f_1^- & ik_2 f_2^+ & -ik_2 f_2^- & ik_3 f_3^+ & -ik_3 f_3^- & ik_4 f_4^+ & -ik_4 f_4^- \\ -k_1^2 & -k_1^2 & -k_2^2 & -k_2^2 & -k_3^2 & -k_3^2 & -k_4^2 & -k_4^2 \\ -k_1^2 f_1^+ & -k_1^2 f_1^- & -k_2^2 f_2^+ & -k_2^2 f_2^- & -k_3^2 f_3^+ & -k_3^2 f_3^- & -k_4^2 f_4^+ & -k_4^2 f_4^- \\ -ik_1^3 & ik_1^3 & -ik_2^3 & ik_2^3 & -ik_3^3 & ik_3^3 & -ik_4^3 & ik_4^3 \\ -ik_1^3 f_1^+ & ik_1^3 f_1^- & -ik_2^3 f_2^+ & ik_2^3 f_2^- & -ik_3^3 f_3^+ & ik_3^3 f_3^- & -ik_4^3 f_4^+ & ik_4^3 f_4^- \end{bmatrix}. \quad (20)$$

Normalizing the incident wave on the right propagating wave before the junction by putting $a_{1,I}^+ = 1$ and applying boundary conditions $a_{j,I}^- = a_{j,II}^+ = 0$ for $j \neq 1$ to suppress the non normalizable plane wave functions. Therefore, the transmission T and the reflection probabilities R are given by

$$T = |a_{j,II}^+|^2, \quad R = |a_{j,I}^-|^2. \quad (21)$$

The numerical results of the transmission probability for ABCA-TTLG is depicted in Fig. 10. At normal inci-

dence, i.e. $ky = 0$ ($\phi = 0$), the transmission equals zero independently of energy or height of the step. There are four high-transmission regions for $E < V$ (see Fig. 10 bottom row), which are typical for tetralayer graphene, shifted away from each other and each one forms a Klein (KT) and anti-Klein (AKT) tunneling region. The expected angles ($\phi = \pm\pi/8, \pm3\pi/8$) for KT and ($\phi = 0, \pm\pi/4$) for ATK (see Fig. 10 top row), which are in agreement with those obtained by Ben *et al.*¹⁵

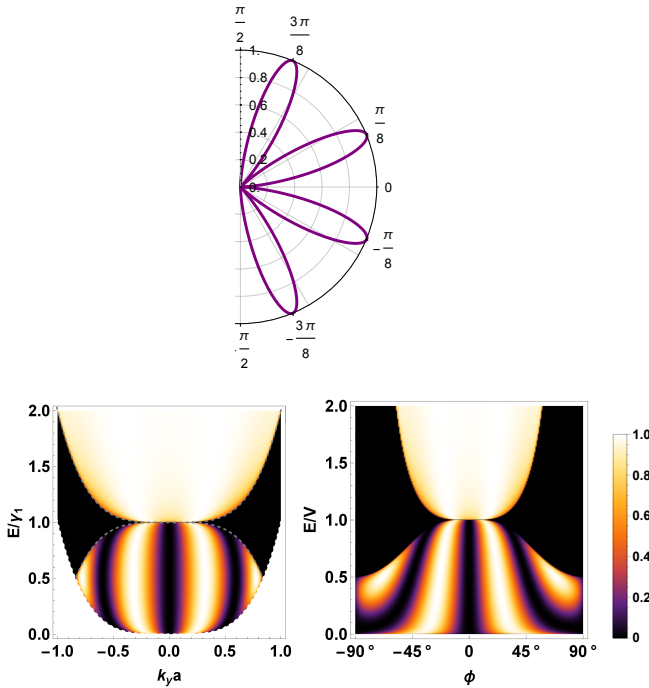


FIGURE 10: (Color online) Transmission probability through a pn junction of height $V = 2E$ in ABCA-TTLG using the two band Hamiltonian in Eq. 11. The top row shows the transmission dependence on the angle. The bottom row shows the counterplots of the transmission versus of the energy, transverse wave vector and angle.

V. CONCLUSION

In conclusion, we have analyzed the band structure, DOS and transmission in ABCA-TTLG. Tight binding Hamiltonian containing nearest-neighbors t and t' , effective Hamiltonian and two band approximation Hamiltonian with interlayer potential difference parameters have been employed. The expressions of band gaps around the \mathbf{k} are obtained. Interlayer potential difference U_0 is found to be responsible for generating band gaps near Dirac point in ABCA-TTLG. The next nearest-neighbor hopping t' breaks the symmetry of Bravais lattice and the corresponding BZ (e.g. its high symmetry points such as corners K and K' move) and the Dirac points may merge and move away from the high symmetry points. This gives rise to 1D-like VHS in the DOS. Using the two-band approximation model, the KT and AKT angles are obtained.

VI. ACKNOWLEDGEMENT

The generous support provided by the Saudi Center for Theoretical Physics (SCTP) is highly appreciated by all authors.

-
- * Electronic address: elmouhafid@gmail.com
† Electronic address: a.jellal@ucd.ac.ma
- ¹ M. Aoki and H. Amawashi, Solid State Commun. 142, 123 (2007).
 - ² M. S. Dresselhaus and G. Dresselhaus, Advances in Physics 51, 186 (2002).
 - ³ M. Koshino and T. Ando, Solid State Commun. 149, 1123 (2009).
 - ⁴ S. H. Jhang, M. F. Craciun, S. Schmidmeier, S. Tokumitsu, S. Russo, M. Yamamoto, Y. Skourski, J. Wosnitza, S. Tarucha, J. Eroms, and C. Strunk Phys. Rev. B 84, 161408(R) (2011).
 - ⁵ M. Koshino, Phys. Rev. B 81, 125304 (2010).
 - ⁶ C. H. Lui, Z. Q. Li, Z. Y. Chen, P. V. Klimov, L. E. Brus, and T. F. Heinz, Nano Lett. 11, 164 (2011).
 - ⁷ S. Latil and L. Henrard, Phys. Rev. Lett. 97, 036803 (2006).
 - ⁸ M. Koshino, Phys. Rev. B 81, 125304 (2010).
 - ⁹ A. I. Cocemasov, D. L. Nika, and A. A. Balandin, Phys. Rev. B 88, 035428 (2013).
 - ¹⁰ K. F. Mak, J. Shan, and T. F. Heinz, Phys. Rev. Lett. 104, 176404 (2010).
 - ¹¹ F. Guinea, A. H. C. Neto, and N. M. R. Peres, Phys. Rev. B 73, 245426 (2006).
 - ¹² A. A. Avetisyan, B. Partoens, and F. M. Peeters, Phys. Rev. B 80, 195401 (2009).
 - ¹³ A. A. Avetisyan, B. Partoens, and F. M. Peeters, Phys. Rev. B 81, 115432 (2010).
 - ¹⁴ C. L. Lu, C. P. Chang, Y. C. Huang, R. B. Chen, and M. L. Lin, Phys. Rev. B, 73, 144427 (2006).
 - ¹⁵ B. Van Duppen and F. M. Peeters, Europhys. Lett. 102, 27001 (2013).
 - ¹⁶ Raad Chegel, Synthetic Metals 223, 172 (2017).
 - ¹⁷ Lei Hao and L. Sheng, Solid State Commun. 149, 1962 (2009).
 - ¹⁸ S. Bala Kumar and Jing Guo, Appl. Phys. Lett. 98, 222101 (2011).
 - ¹⁹ E. McCann and V. I. Fal'ko, Phys. Rev. Lett. 96, 086805 (2006).
 - ²⁰ E. McCann, D. S. L. Abergel, and V. I. Fal'ko, Solid State Commun. 75, 193402 (2007).
 - ²¹ Y. Hasegawa, R. Konno, H. Nakano, and M. Kohmoto Phys. Rev. B 74, 033413 (2006).
 - ²² P. Dietl, F. Piéchon, and G. Montambaux, Phys. Rev. Lett. 100, 236405, (2008).
 - ²³ B. Wunsch, F. Guinea, and F. Sols, New J. Phys. 10, 103027 (2008).
 - ²⁴ M. Koshino, New J. Phys. 11 095010 (2009).
 - ²⁵ B. Van Duppen, S. H. R. Sena, and F. M. Peeters, Phys. Rev. B 87, 195439 (2013).
 - ²⁶ H. Min and A. H. MacDonald, Phys. Rev. B 77, 155416 (2008).
 - ²⁷ M. Nakamura and L. Hirasawa, Phys. Rev. B 77, 045429 (2008).